Inorganica Chimica Acta 384 (2012) 83–96

Contents lists available at SciVerse ScienceDirect

Inorganica Chimica Acta

journal homepage: www.elsevier.com/locate/ica

Studies on the effect of metal ions of hydrazone complexes on interaction with nucleic acids, bovine serum albumin and antioxidant properties

Palanisamy Sathyadevi [a], Paramasivam Krishnamoorthy [a], Eswaran Jayanthi [a], Rachel R. Butorac [b], Alan H. Cowley [b], Nallasamy Dharmaraj [a,*]

[a] Department of Chemistry, Bharathiar University, Coimbatore 641046, India
[b] Department of Chemistry and Biochemistry, University of Texas at Austin, Austin, TX 78712, USA

ARTICLE INFO

Article history:
Received 15 August 2011
Received in revised form 11 November 2011
Accepted 12 November 2011
Available online 19 November 2011

Keywords:
DNA binding
Protein binding
Hydrazones
Transition metal complexes
Crystal structure
Antioxidant properties

ABSTRACT

Three new transition metal complexes of the type ML_2 (where M = Ni(II), Co(II) or Cu(II); HL = *N′*-[phenyl(pyridin-2-yl)methylidene]furan-2-carbohydrazide]) have been prepared by treating $[NiCl_2(PPh_3)_2]$, $[CoCl_2(PPh_3)_2]$ or $[CuCl_2(PPh_3)_2]$ with *N′*-[phenyl(pyridin-2-yl)methylidene]furan-2-carbohydrazide derived from furoic acid hydrazide and 2-benzoyl pyridine wherein the hydrazone ligand (**L**) coordinated to the respective metal ions in 1:2 stoichiometry to mononuclear octahedral complex. The crystal structure of the complexes $[NiL_2]$ (**1**), $[CoL_2]$ (**2**) and $[CuL_2]$ (**3**) solved using single crystals revealed a distorted octahedral geometry around the metal ion involving the coordination of an azomethine nitrogen, a pyridine nitrogen and an enolic oxygen derived from deprotonation of the ligand. From the bioinorganic application point of view, a detailed work on the binding of the complexes **1**, **2** and **3** with CT DNA as well as BSA was undertaken along with DNA cleavage. *In vitro* assay on the antioxidant activity of the above complexes and hydrazone ligand revealed that they possess significant antioxidant activity. However, among the newly synthesized hydrazone complexes, complex **3** having coordinated Cu^{2+} ion in its molecular structure exhibited superior activity in all the biological studies in comparison with the other two complexes possessing nickel and cobalt ions with same ligand (**L**).

1. Introduction

Recent years have witnessed an unprecedented progress in biological applications of inorganic pharmaceuticals because of their key role in clinical therapy. Important examples include *cis*-platin and corresponding second generation alternatives such as oxaliplatin and carboplatin those serve as chemotherapeutic agents for solid malignancies and as diagnostic contrast agents such as MRI [1–3]. Transition metals are particularly suitable for this purpose because they can adopt a wide variety of coordination numbers, geometries and oxidation states in comparison with carbon and other main group elements [4]. We were particularly attracted to the transition metal complexes of aryl hydrazones because such compounds have been reported to function as antibacterial, antiviral and antifungal agents [5–8]. A further reason for using metal-containing compounds as structural scaffolds relates to the kinetic stabilities of their coordination spheres in the biological environment [9].

Investigation of the interactions of DNA with small molecules can serve as a foundation for the design of new types of pharmaceutical molecules. The development of interaction models and the elucidation of the mechanisms of interaction of transition metal complexes with DNA and their subsequent applications in molecular biology continue to attract significant attention. In particular, considerable interest has been generated in DNA binding and DNA cleavage by redox and photoactive metal complexes in order to explore the sequence specificities of DNA binding using a variety of intercalating ligands [10–12]. Moreover, certain metal complexes have been shown to be capable of cleaving DNA strands. In the case of cancer genes, the cleavage of the DNA double strands can destroy their replication ability. Free radicals can adversely affect lipids, proteins and DNA and have been implicated in the aging process and in a number of human diseases. Antioxidants are capable of neutralizing these reactive species in terms of prevention, interception and damage repair.

Serum albumin is the most abundant protein in animals including human circulatory system that is in-charge for the transport, distribution and deposition of a variety of endogenous and exogenous substances in body [13]. Knowledge of interaction mechanisms between drugs and plasma proteins is very important to understand the pharmacodynamics and pharmacokinetics of a drug. Drug binding influences their distribution, excretion, metabolism and interaction with the target tissues [14]. Bovine serum albumin (BSA) has been proven to have a high homology and a similarity to human serum albumin (HSA) in sequence and

* Corresponding author. Tel.: +91 422 2428316; fax: +91 422 2422387.
E-mail address: dharmaraj@buc.edu.in (N. Dharmaraj).

0020-1693/$ - see front matter © 2011 Elsevier B.V. All rights reserved.
doi:10.1016/j.ica.2011.11.033

conformation [15]. Therefore, it is always selected as a particularly relevant protein and has become the best-studied model of general drug–protein interactions.

It has been reported that hydrazone complexes of transition metals exhibit DNA interactions, DNA cleavage, as well as antitumor and antimicrobial properties [16–19], but it appeared that very less attention was only being paid so far to investigate systematically the protein binding ability of such similar systems. However, to the best of our knowledge, there was no literature available on the synthesis, structural characterization and interaction studies of Ni(II), Co(II) and Cu(II) complexes containing *N′*-[phenyl(pyridin-2-yl)methylidene]furan-2-carbohydrazide as ligand. The foregoing facts stimulated our interest on the syntheses, structure, DNA binding, cleavage, protein binding and antioxidant properties of bivalent Ni, Co and Cu complexes containing the above hydrazide ligand. The structures of the new complexes were established on the basis of single-crystal X-ray diffraction studies and spectroscopic data. In addition, detailed investigations on the effect of metal ions on the biological potential of the hydrazone complexes were also undertaken.

2. Experimental

2.1. Materials and physical measurements

The following reagent grade chemicals were procured commercially and used without subsequent purification: $NiCl_2{\cdot}6H_2O$, $CoCl_2{\cdot}6H_2O$, $CuCl_2{\cdot}2H_2O$ and triphenylphosphine (Sigma–Aldrich); furoic acid hydrazide and benzoyl pyridine (Alfa Aesar), 2,2′-azino-3-ethylbenzthiazoline-6-sulfonic acid diammonium salt, 1-1′-diphenyl-2-picrylhydrazyl, 2-thiobarbituric acid, 2,4,6-tripyridyl-*S*-triazine (Sigma–Aldrich). Calf-thymus (CT DNA) and bouvine serum albumin (BSA) were purchased from Himedia. The plasmid supercoiled (SC) pUC19 DNA was purchased from Bangalore GeNei, Bangalore, India. All other chemicals and reagents used for biological studies were obtained commercially.

Microanalyses (% C, H and N) were performed on a Vario EL III CHNS analyzer and all IR spectra were recorded as KBr pellets on a Nicolet Avatar instrument in the frequency range 400–4000 cm^{-1}. The ^1H NMR spectrum of the ligand was recorded on a Bruker AMX 500 spectrometer operating at 500 MHz and using tetramethylsilane as the internal standard. The chemical shift ratios are reported in parts per million (ppm) relative to $SiMe_4$ (δ 0.00). The electronic absorption and emission spectra were recorded in DMSO:buffer (1:99) solution on Jasco V-630 spectrophotometer and Jasco FP 6600 spectrofluorometer, respectively. The cyclic voltammetric study was carried out with a CH Instruments electrochemical analyzer in dichloromethane using tetrabutylammonium perchlorate (TBAP) as the supporting electrolyte. A three-electrode configuration cell comprising a glassy carbon working electrode, a platinum wire auxiliary electrode and an Ag/AgCl reference electrode was employed in this study. All solutions were purged with nitrogen gas prior to making measurements at room temperature.

2.2. Syntheses of metal–hydrazone complexes

The requisite precursor metal complexes $[NiCl_2(PPh_3)_2]$, $[CoCl_2(PPh_3)_2]$ and $[CuCl_2(PPh_3)_2]$ and the ligand *N′*-[phenyl(pyridin-2-yl)methylidene]furan-2-carbohydrazide (H-FBP) (**HL**) were prepared according to the literature methods [20–22].

2.2.1. Synthesis of $[Ni(L)_2]$ (**1**)

Complex $[Ni(FBP)_2]$ (**1**) was prepared by refluxing equimolar quantities of the ligand (H-FBP) (0.291 g; 1 mM) and $[NiCl_2(PPh_3)_2]$ (0.653 g; 1 mM) in 40 mL of methanol (Scheme 1). After 30 min, a few drops of methanolic KOH were added to the reaction mixture, following which it was refluxed for an additional 5 h. After cooling the reaction mixture to room temperature, the resulting precipitate was filtered, washed with methanol and dried in vacuo for 24 h. Following a purity check by TLC, crystals of **1** suitable for single-crystal X-ray diffraction studies were obtained by recyrstallization from a $MeOH/CHCl_3$ solvent mixture. Yield: 47%. Color: dark brown, mp: 270–272 °C. *Anal.* Calc. for $NiC_{34}H_{32}N_6O_8$ (Mol. Wt. = 711.35): C, 57.40; H, 4.53; N, 11.81. Found: C, 57.24; H, 4.81; N, 11.52%. Selected IR bands (ν_{max}/cm^{-1}): 1587 & 1501 (C=N–N=C); 1309 (C–O); 1084 (N–N).

2.2.2. Synthesis of $[Co(L)_2]$ (**2**)

The complex $[Co(L)_2]$ (**2**) was prepared from $[CoCl_2(PPh_3)_2]$ (0.653 g; 1 mM) and the ligand (H-FBP) (0.291 g; 1 mM) using a similar procedure to that described for **1** (Scheme 1). Slow evaporation of a $MeOH/CHCl_3$ solution of **2** afforded a crop of brown crystals suitable for X-ray diffraction study. Yield: 48% mp: 280–282 °C. *Anal.* Calc. for $CoC_{34}H_{26}N_6O_5$ (Mol. wt. = 657.540): C, 62.10; H, 3.98; N, 12.78. Found: C, 61.94; H, 3.91; N, 12.96%. Selected IR bands (ν_{max}/cm^{-1}): 1586 & 1497 (C=N–N=C); 1311 (C–O); 1078 (N–N).

2.2.3. Syntheses of $[Cu(L)_2]$ (**3**) and $[Cu(Cl)(PPh_3)_3]$ (**3a**)

Complex **3** $[Cu(FBP)_2]$ was prepared from $[CuCl_2(PPh_3)_2]$ (0.658 g; 1 mM) and the (H-FBP) ligand (0.291 g; 1 mM) using a similar procedure to that described for **1** (Scheme 1). However, analysis of the product by TLC revealed the presence of two different complexes, namely **3** and **3a**. Complex **3** was eluted from the column using a 75:25 petroleum ether and ethyl acetate mixture as the eluent. Slow evaporation of a $MeOH/CHCl_3$ solution of **3** afforded a crop of violet crystals suitable for X-ray diffraction study. Yield: 38%, mp: 276–278 °C. *Anal.* Calc. for $CuC_{35}H_{28}N_6O_5$ (Mol. wt. = 676.180): C, 62.17; H, 4.17; N, 12.42. Found: C, 61.95; H, 4.04; N, 12.53%. Selected IR bands (ν_{max}/cm^{-1}): 1584 & 1505(C=N–N=C); 1309 (C–O); 1082 (N–N).

Complex **3a** was obtained by using an 85:15 petroleum ether/ethyl acetate mixture as the eluent. A crop of crystals suitable for single crystal X-ray diffraction study was obtained in a similar fashion to that described above for **3**. The structure of **3a** was shown to identical to that of $[Cu(Cl)(PPh_3)_3]$ [23].

2.3. X-ray crystallography

For each compound, a crystal of suitable quality was removed from a vial, covered with mineral oil and mounted on a nylon thread loop. The X-ray diffraction data for compounds **1**, **2** and **3a** were collected on a Rigaku AFC-12 Saturn 724+CCD diffractometer equipped with a graphite-monochromated Mo Kα radiation source (λ = 0.71073 Å) and a Rigaku XStream low-temperature device cooled to 100 K. The X-ray diffraction data for complex **3** were collected on a Rigaku SCX-Mini diffractometer equipped with a Mercury CCD, a graphite-monochromated Mo Kα radiation source (λ = 0.71073 Å) and a Rigaku Tech50 low-temperature device cooled to 223 K. Corrections were applied for Lorentz and polarization effects for each compound. Each structure was solved by direct methods and refined by full-matrix least-squares cycles on F^2 using the Siemens SHELXTL PLUS 5.0 (PC) software package [24,25] and PLATON [26]. All non-hydrogen atoms were refined anisotropically and hydrogen atoms were placed in fixed, calculated positions using a riding model.

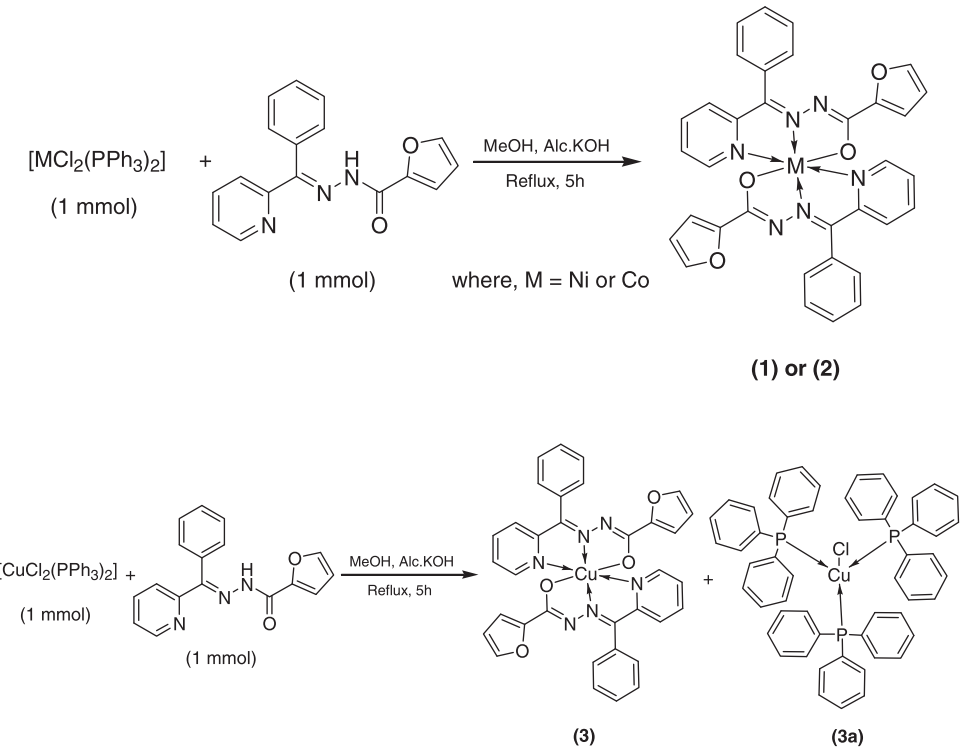

Scheme 1. Synthesis of complexes **1**, **2**, **3** and **3a**.

2.4. DNA binding experiments

2.4.1. Electronic absorption titration

Electronic absorption titrations were performed with a fixed concentration of metal complexes (25 μM) but by varying nucleotide concentration from 0 to 25 μM. The absorbance (A) band of the complexes that get shifted significantly due to the addition of CT DNA was chosen to monitor as an indication of the binding between them. From the absorption titration data, the intrinsic binding constant (K_b) of the metal complexes with CT DNA was determined using the equation [27],

$$[\mathrm{DNA}]/[\varepsilon_a - \varepsilon_f] = [\mathrm{DNA}]/[\varepsilon_b - \varepsilon_f] + 1/K_b[\varepsilon_b - \varepsilon_f]$$

where, [DNA] is the concentration of DNA in base pairs, ε_a is the extinction coefficient of the complex at a given DNA concentration, ε_f is the extinction coefficient of the complex in free solution and ε_b is the extinction coefficient of the complex when fully bound to DNA. A plot of $[\mathrm{DNA}]/[\varepsilon_b - \varepsilon_f]$ versus [DNA] gave a slope and an intercept equal to $1/[\varepsilon_a - \varepsilon_f]$ and $(1/K_b)[\varepsilon_b - \varepsilon_f]$, respectively. The intrinsic binding constant K_b is the ratio of the slope to the intercept.

2.4.2. Competitive binding fluorescence measurements

The apparent binding constant (K_{app}) of the complexes was determined by fluorescence spectral technique using ethidiumbromide (EB)-bound CT DNA solution in Tris–HCl buffer (pH, 7.2). The changes in fluorescence intensities at 605 nm (545 nm excitation) of EB bound to DNA were measured with respect to concentration of the complex. EB was non-emissive in Tris–HCl buffer solution (pH 7.2) due to fluorescence quenching of the free EB by the solvent molecules. In the presence of DNA, EB showed enhanced emission intensity due to its intercalative binding to DNA. A competitive binding of the metal complexes to CT DNA resulted in the displacement of the bound EB, thereby decreasing its emission intensity. The quenching constant (K_q) was calculated using the classical Stern–Volmer equation [28]: $I_0/I = K_q\ [Q] + 1$; I_0 is the emission intensity in the absence of quencher, I is the emission intensity in the presence of quencher, K_q is the quenching constant, [Q] is the quencher concentration (10 μM). K_q is the slope, obtained from the plot of I_0/I versus [Q]. The apparent binding constant (K_{app}) has been calculated from the equation, K_{EB} [EB] = K_{app}[complex] with [EB] = 10 μM and $K_{EB} = 1 \times 10^7\ M^{-1}$.

2.5. DNA cleavage experiments

The extent of DNA cleavage induced by the test compounds was monitored by agarose gel electrophoresis. A solution containing 25 μL of pUC19 DNA (1 μg), HCl (50 mM, pH 7.2), NaCl (50 mM), the metal complex (35 μM), and H_2O_2 (60 μM) was incubated at 37 °C for 1 h. Subsequently, 4 μL of 6× DNA loading buffer containing 0.25% bromophenol blue, 0.25% xylene cyanol and 60% glycerol was added to the test solution and then mixed with 1% agarose gel containing 1.0 μg/mL of ethidium bromide. Electrophoresis was performed at 5 V/cm for 2 h in a TBE buffer and the bands were visualized under UV light and photographed. The cleavage efficiencies were measured by determination of the ability of each complex to convert the super coiled DNA (SC) to the open circular form (OC). After electrophoresis, the proportion of both the cleaved and uncleaved DNA in each fraction was quantitatively estimated on the basis of the band intensities using the BIORAD Gel Documentation System. The intensity of each band relative to that of the plasmid supercoiled form was multiplied by 1.43 to take account of the reduced affinity for ethidium bromide [29].

2.6. Protein binding studies

Binding of metal hydrazone complexes with bovine serum albumin (BSA) was studied using fluorescence spectra recorded with excitation at 280 nm and corresponding emission at 345 nm assignable to that of bovine serum albumin (BSA). The excitation

and emission slit widths and scan rates were constantly maintained for all the experiments. Samples were carefully degassed using pure nitrogen gas for 15 min by using quartz cells ($4 \times 1 \times 1$ cm) with high vacuum Teflon stopcocks. Stock solution of BSA was prepared in 50 mM phosphate buffer (pH 7.2) and stored in the dark at 4 °C for further use. Concentrated stock solutions of metal complexes were prepared by dissolving them in DMSO: phosphate buffer (1:99) and diluted suitably with phosphate buffer to required concentrations. 2.5 ml of BSA solution (μM) was titrated by successive additions of a 25 μl stock solution of complexes (10^{-4} M) using a micropipette. Synchronous fluorescence spectra was also recorded using the same concentration of BSA and complexes as mentioned above with two different Δλ (difference between the excitation and emission wavelengths of BSA) values such as 15 and 60 nm.

2.7. Antioxidant assays

The free radical (DPPH, ABTS, FRAP, OH and NO) scavenging activities of the samples were determined according to the reported methods [30–34]. The lipid peroxidation was evaluated by the modified method of Druper and Hadly *in ex vivo* and it was determined on the basis of the formation of thiobarbituric acid-reactive substances by an iron/ascorbate system with liver microsomes [35,36]. For each of the above assays, the tests were run in triplicate and various concentrations of the complexes were used to fix a concentration at which each complex showed approximately 50% activity. The percentage activities were calculated using the formula, % activity = $[(A_0 - A_C)/A_0] \times 100$ where A_0 and A_C represent the absorbance in the absence and presence of the tested complex, respectively. The 50% activity (IC_{50}) can be calculated using the percentage of activity results.

3. Results and discussion

The analytical data obtained for the metal hydrazone complexes **1**–**3** are in satisfactory agreement with the proposed structures and it is clear that in each case the hydrazone ligand coordinates to the metal ion in 1:2 instead of 1:1 M ratio.

3.1. X-ray crystallography

3.1.1. Crystal structure of $[Ni(L)_2]$ (**1**)

The molecular structure of complex **1** is depicted in Fig. 1 along with the atom labeling scheme. The crystallographic data and pertinent bond lengths and angles are listed in Tables 1 and 2. Compound **1** crystallizes in the monoclinic space group $P2_1/n$. The Ni(II) center possesses a distorted octahedral geometry that comprises two equivalent monoanionic ligands that are coordinated in a meridional fashion such that the *cis* pyridyl nitrogen, the *trans* azomethine nitrogen and *cis* enolate oxygen atoms are essentially perpendicular to each other.

Due to keto-enol tautomerism it is well known that the imino tautomers can exist as two geometrical isomers, namely the *syn* (Z) and *anti* (E) forms. However, in this case, only the E isomer is observed. The torsion angle of 178.6(2)° for C5–C6–N2–N3 and 178.0(2)° for C22–C23–N5–N6 support the view that the ligands adopt the E conformation upon coordination [37]. The coordination environment around the nickel center is distorted octahedral and comprises two oxygen and four nitrogen atoms. The ligand–metal–ligand bite angles are 79.00(9)° [N1–Ni1–N2], 77.32(8)° [N2–Ni1–O1], 77.42(9)° [N5–Ni1–O3] and 79.04(9)° [N4–Ni1–N5]. The two central coordinating bonds Ni1–N1 [2.077(2)] and Ni1–O1 [2.083(2)] are comparable in length to those of the basal planar bonds Ni1–O3 [2.083], Ni1–N5 [1.985(2)], Ni1–N4 [2.084(3)] and Ni1–N2 [1.991(2)]. The [N2–Ni1–N5] trans angle is 176.9(1)°, whereas the other trans angles [N1–Ni1–O1] 156.31(8)° and [N4–Ni1–O3] 156.39(8)° are constrained within the meridional ligands. The forgoing observations suggest that the coordination geometry is considerably distorted from that of a perfect octahedron [38]. The Ni(II) center is shared by four fused five-membered chelate rings and the bicyclic chelate system {Ni1O3C30N6N5C23C22} with its counterpart {Ni1O1C13N3N2C6C5N1}. One of the furan moieties attached to the Ni(II) center was found to be disordered with respect to rotation about the C30 to C31 bond. The asymmetric unit also contains four solvated water molecules. One of the hydrogens on O8 could not be located in the difference map hence it was not included in the ORTEP diagram. The crystal–packing diagram evidences substantial H-bonding. A perspective view of the unit cell packing and the hydrogen bond network of **1** are shown in Fig. S1.

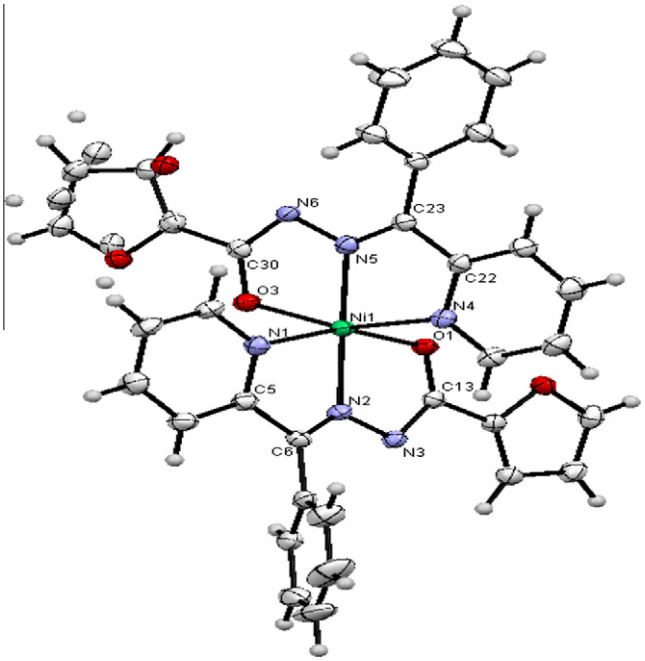

Fig. 1. Molecular structure of complex **1** showing the atom-numbering scheme with ellipsoid of 50% probability and solvent molecules were omitted for clarity.

3.1.2. Crystal structure of $[Co(L)_2]$ (**2**)

The X-ray crystal structure of $[Co(L)_2]$ (**2**) is presented as an ORTEP diagram in Fig. 2 along with an atom numbering scheme. Listings of pertinent bond distances and angles are presented in Tables 1 and 2. Analogously to the complex **1**, the Co atom in complex **2** is hexacoordinated by two units of the tridentate hydazone ligand. Two monodeprotonated ligands coordinate to the Co(II) center in a tridentate fashion and feature enolate O, azomethine N and pyridine N-donor atoms.

The Co(II) center is shared by four fused five-membered chelate rings and the bicyclic chelate system {Co1O3C31N6N5C23C24} with its counterpart {Co1O1C13N3N2C6C5N1}. Furthermore, one of the furan moieties attached to the Co(II) center is disordered by rotation about the C31–C32 bond. The observed torsion angles of −176.9(2)° for C5–C6–N2–N3, and −175.0(2)° for C23–C24–N5–N6 imply that the ligand adopts the E-conformation upon coordination. The coordination environment around the cobalt atom is distorted octahedral and the two oxygen atoms and four nitrogen atoms occupy the coordination sites with varying ligand–metal–ligand bite angles; 78.50(7)° [N1–Co1–N2], 76.98(6)° [N2–Co1–O1], 78.37(6)° [N5–Co1–O3] and 78.72(7)° [N4–Co1–N5]. The two central bonds Co1–N1 [2.099(2)] and Co–O1

Table 1
Crystal data and structure refinement data.

Empirical formula	$C_{34}H_{32}N_6NiO_8$ (**1**)	$C_{34}H_{26}CoN_6O_5$ (**2**)	$C_{35}H_{28}CuN_6O_5$ (**3**)
Name	$[Ni(FBP)_2]\cdot 3H_2O\cdot(OH)$	$[Co(FBP)_2]\cdot H_2O$	$[Cu(FBP)_2]\cdot MeOH$
Formula weight	711.37	657.54	676.17
Crystal system	monoclinic	monoclinic	orthorhombic
Space group	$P2_1/n$	$P2_1/c$	*Pbca*
T (K)	100(2)	100(2)	223(2)
Wavelength (Å)	0.71075	0.71075	0.71069
Unit cell dimensions			
a (Å)	8.7518(9)	10.9462(5)	15.3886(6)
b (Å)	27.268(3)	14.8724(7)	19.6995(7)
c (Å)	14.0131(15)	18.6278(9)	20.7510(8)
α (°)	90.000	90.000	90.000
β (°)	95.189(3)	102.0440(10)	90.000
γ (°)	90.000	90.000	90.000
Colour	dark brown	brown	violet
D_{calc} (Mg/m3)	1.419	1.473	1.428
Z	4	4	8
$F(0\,0\,0)$	1480	1356	2792
Crystal size (mm3)	$0.21 \times 0.20 \times 0.09$	$0.30 \times 0.18 \times 0.16$	$0.18 \times 0.13 \times 0.10$
hkl limits	$-11 \leqslant h \leqslant 11$	$-14 \leqslant h \leqslant 14$	$-19 \leqslant h \leqslant 19$
	$-35 \leqslant k \leqslant 35$	$-19 \leqslant k \leqslant 19$	$-25 \leqslant k \leqslant 25$
	$-18 \leqslant l \leqslant 8$	$-24 \leqslant l \leqslant 24$	$-26 \leqslant l \leqslant 26$
θ range for data collection	3.01–27.49°	3.22–27.46°	3.01–27.48°
Reflections collected	33 288	78 524	64 182
R indices (all data)	$R_1 = 0.0798$	$R_1 = 0.0457$	$R_1 = 0.0852$
	$wR_2 = 0.1268$	$wR_2 = 0.1133$	$wR_2 = 0.1146$
Data/restraints /parameters	7633/142/489	6771/149/462	7205/0/429
Independent reflections	7633 [R(int) = 0.0582]	6771 [R(int) = 0.0361]	7205 [R(int) = 0.0939]
Goodness-of-fit (GOF) on F^2	1.041	0.951	1.055

Table 2
Selected bond lengths (Å) and bond angles (°) for **1** and **2**.

$C_{34}H_{32}N_6NiO_8$ (**1**)				$C_{34}H_{26}CoN_6O_5$ (**2**)			
Bond lengths		Bond angles		Bond lengths		Bond angles	
Ni1–N1	2.077(2)	N2–Ni1–O1	77.32(8)	Co1–N1	2.099(2)	N2–Co1–O1	76.98(6)
Ni1–N2	1.991(2)	N2–Ni1–N1	79.00(9)	Co1–N2	1.973(2)	N2–Co1–N1	78.50(7)
Ni1–O3	2.074(2)	N1–Ni1–N5	99.36(9)	Co1–O3	2.069(1)	N1–Co1–N5	96.98(7)
Ni1–N5	1.985(2)	N5–Ni1–O1	104.33(8)	Co1–N5	1.956(2)	N5–Co1–O1	107.32(6)
Ni1–N4	2.084(3)	N5–Ni1–O3	77.42(9)	Co1–N4	2.057(2)	N5–Co1–O3	78.37(6)
Ni1–O1	2.083(2)	N5–Ni1–N4	79.04(9)	Co1–O1	2.105(1)	N5–Co1–N4	78.72(7)
		O3–Ni–N4	156.39(8)			O3–Co1–N4	157.08(6)
		N4–Ni1–O1	90.50(8)			N4–Co1–O1	90.55(6)
		N1–Ni1–N4	93.67(9)			N1–Co1–N4	90.00(7)
		N1–Ni1–O1	156.31(8)			N1–Co1–O1	155.32(6)
		N5–Ni1–N2	176.93(1)			N5–Co1–N2	174.46(7)

[2.105(1)] are comparable in length to those of the basal planar bonds Co1–O3 [2.069(1)], Co1–N5 [1.956(2)], Co1–N4 [2.057(2)] and Co1–N2 [1.973(2)]. The foregoing bond distances imply that all the axial and basal planar bonds are essentially equal in length. The [N2–Co1–N5] *trans* angle is 174.46(7)°; however, the *trans* angles of 155.32(6)° [N1–Co1–O1] and 157.08(6)° [N4–Cl1–O3] are constrained within the meridional ligands. These observations suggest that the coordination geometry is significantly distorted from that of a perfect octahedron. A perspective view of the unit cell packing and the hydrogen bond network of **2** are shown in Fig. S2.

3.1.3. Crystal structure of $[Cu(L)_2]$ (**3**)

An ORTEP diagram of the structure of **3** is displayed in Fig. 3. The crystallographic data, along with a selection of bond lengths and bond angles, are presented in Tables 1 and 3, respectively. The X-ray study of complex **3** revealed that the crystals are comprised of orthorhombic unit cells in the space group *Pbca* with $Z = 8$. The unit cell dimensions are $a = 15.3886(6)$ Å, $b = 19.6995(7)$ Å, $c = 20.7510(8)$ Å, $\alpha = \beta = \gamma = 90°$, $V = 6290.6(4)$ Å^3, $D_{calc} = 1.428$ μg/m^3. The formula for the complex in crystalline form is $C_{35}H_{28}Cu_1N_6O_5$. The Cu(II) coordination environment is distorted octahedral as evident from the bond angles subtended at the metal center. The basal plane comprises an imine nitrogen (N2), an enolate oxygen (O2), an imine nitrogen (N6) and an pyridyl nitrogen N(5). The pyridyl N1 and enolate O1 atoms occupy the apical positions thus completing the distorted octahedral coordination environment.

The coordination environment around Cu(II) is distorted as evidenced by the observation that the bite angles for the two oxygen and four nitrogen atoms vary between 75.97(9)° [N1–Cu1–N2], 74.59(8)° [N2–Cu1–O1], 79.54(9)° [N5–Cu1–N6] and 79.34(8)° [N6–Cu1–O2]. The observed torsion angles of −177.5(2)° for C5–C6–N2–N3 and −176.6(2)° for C23–C24–N6–N7 imply that the ligand is coordinated to the metal in the *E* conformation [39]. The environment around the metal is distorted octahedral and comprises two equivalent monoanionic ligands that are coordinated in a tridentate fashion and orientated such that they are essentially perpendicular to each other. The two central bonds Cu1–N1 [2.267(2)] and Cu1–O1 [2.295(2)] are comparable in length to those of the basal planar bonds. In turn, this implies that

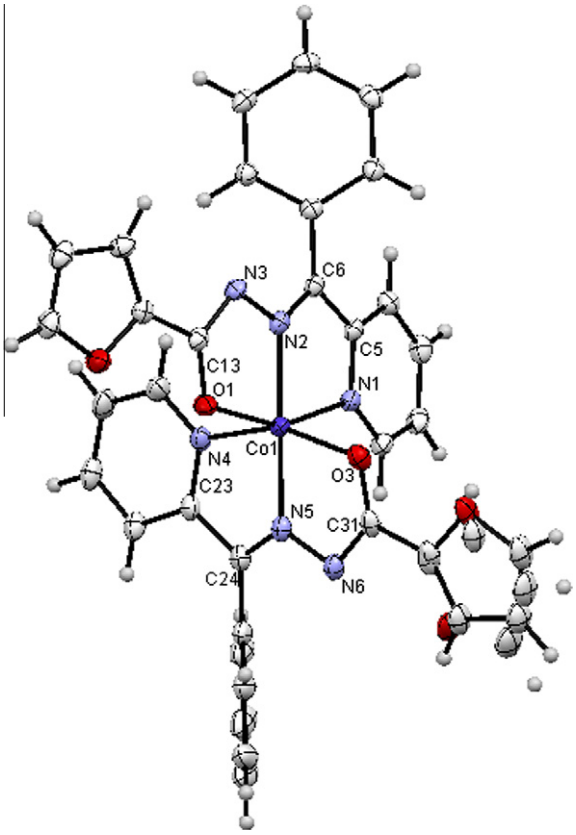

Fig. 2. Molecular structure of complex **2** showing the atom-numbering scheme with ellipsoid of 50% probability and solvent molecules were omitted for clarity.

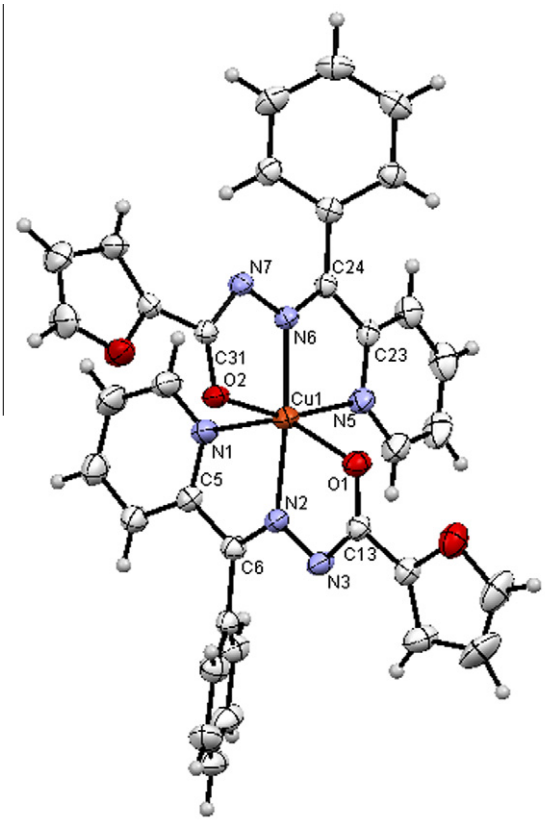

Fig. 3. Molecular structure of complex **3** showing the atom-numbering scheme with ellipsoid of 50% probability and solvent molecules were omitted for clarity.

the Cu(II) complex adopts a tetragonally elongated structure. The *trans* pair of bonds Cu1–N1 and Cu1–O1 are longer than the remaining four bonds Cu1–N2, Cu1–O2, Cu1–N5 and Cu1–N6. This distortion is a consequence of the Jahn–Teller effect that operates in the d^9 electronic ground state of the six-coordinate complex. In this case, one *trans* pair of coordinate bonds is elongated while the remaining four bonds are shortened. It is clear from the bond angles, N1–Cu1–N2 [75.97(9)°], N2–Cu1–O1 [74.59(8)°], O2–Cu1–N6 [79.34(8)°] and N6–Cu1–N5 [79.54(9)°] that the coordination geometry departs considerably from that of a perfect octahedron. The Cu–N(py), Cu–N(imine) and Cu–O(enolate) bond lengths fall within the ranges reported for similar complexes of divalent metal ions. In general, the shortest coordinate bonds are those to the central imine N donors. The bonds to the distal pyridyl and carbonyl groups are significantly weaker. The latter observation can be attributed to greater π-back bonding in the Cu–N(imine) bond in comparison with that of the Cu–N(py) bond in concert with the steric requirements of the meridionally coordinated ligand [40]. A solvated methanol is involved in the intermolecular hydrogen bonding between O1 of the enolate oxygen of the hydazone ligand and the H50 hydrogen atom of the solvated methanol molecule. A perspective view of the unit cell packing and the hydrogen bond network of **3** is shown in Fig. S3.

The complex **3a** was obtained as a minor product in the reaction of $[CuCl_2(PPh_3)_2]$ with the hydrazone ligand (HL) and crystallized to get suitable crystals for characterization using XRD. The single crystal XRD data proved that the molecular formula of **3a** is $[CuCl(PPh_3)_3]$ (Fig. S4) without the coordination of the hydrazone moiety. It is understood that the copper ion is reduced to 1+ oxidation state by the hydrazone ligand which is normally a good reducing agent [23]. The crystal structure, unit cell parameters, bond lengths of **3a** was found to be in good agreement with the earlier report.

Table 3
Selected bond lengths (Å) and bond angles (°) for **3**.

$C_{35}H_{28}CuN_6O_5$ (**3**)			
Bond lengths		Bond angles	
Cu1–O1	2.295(2)	O1–Cu1–N2	74.59(8)
Cu1–N2	2.010(2)	N2–Cu1–N1	75.97(9)
Cu1–N1	2.267(2)	N1–Cu1–N6	96.00(9)
Cu1–N6	1.952(2)	N6–Cu1–O1	113.49(8)
Cu1–O2	2.028(2)	N5–Cu1–N6	79.54(9)
Cu1–N5	2.058(2)	N6–Cu1–O2	79.34(8)
		N6–Cu1–N2	171.90(9)
		N1–Cu1–O1	150.35(8)
		O1–Cu1–O2	89.32(7)
		N1–Cu1–O2	93.33(8)
		O2–Cu1–N2	101.92(8)

3.2. Infrared spectra

The IR spectrum of the free ligand was compared with those of the metal complexes in order to study the binding mode(s) of the hydrazone ligand to the metal. The ligand spectrum exhibits characteristic absorption bands at 3143, 1689, 1582 and 1072 cm^{-1} due to the $\nu_{(N-H)}$, $\nu_{(C=O)}$, $\nu_{(C=N)}$ and $\nu_{(N-N)}$ vibrations, respectively. The IR spectra of the complexes revealed significant differences from those of the free ligand as described below. The bands due to the $\nu_{(C=O)}$ and $\nu_{(N-H)}$ stretching vibrations are absent in the IR spectra of the complexes and two new bands appear between 1587–1497 cm^{-1} and 1309–1311 cm^{-1} due to the $\nu_{(C=N-N=C)}$ and $\nu_{(C-O)}$ stretching vibrations, respectively, thus implying that deprotonation of the N–H moiety has occurred, thereby confirming that the hydrazone is coordinated in the enol form. Furthermore, the decrease in the $\nu_{(C=N)}$ stretching frequency involving the azomethine nitrogen indicates that the imine nitrogen is involved in coordina-

tion to the metal ion [41]. The increase in the $\nu_{(N-N)}$ stretching frequency in comparison with that of the free ligand (~5–12 cm^{-1}) is due to the increase in the double bond character offsetting the loss of electron density via donation to the transition metal, thereby providing further confirmation that the coordination of the hydrazone ligand involves the azomethine atom [42].

3.3. Electronic spectra

The electronic spectra of all three complexes (**1**, **2** and **3**), which were recorded in DMSO:buffer solution, exhibit two bands in the range 266–373 nm (Table 4). An intense band that is apparent in the 364–373 nm region can be assigned to an ligand–metal charge transfer (LMCT) transitions of the imine group and the higher energy bands below 300 nm are attributable to $\pi \rightarrow \pi^*$ intraligand transitions [43].

3.4. Photoluminescence studies

The luminescence behavior of complexes **1**, **2**, and **3** was also investigated. When an excitation wavelength corresponding to the highest energy absorption was used, none of the complexes exhibited emission. However, the use of a lower energy excitation wavelength resulted in an intense emission in each case (Table 4). The emission maxima for the complexes fell in the range of 450–500 nm exhibited a positive shift of approximately 70–130 nm in comparison with those of the excitation maxima. The CT luminescence observed for these complexes may be due to the presence of an imine functional group [44]. It is likely that this emission originates from the lowest energy ligand-to-metal charge transfer (LMCT) state. The stronger blue luminescence observed may be due to the coordination of the ligand to the metal center which increases the rigidity of the ligand and reduces the loss of energy via a non-radiative pathway, thus enhancing the probability of a ligand π–π^* transition.

Table 4
Electronic and fluorescence spectral data for metal hydrazone complexes.

Complex	λ_{max}(nm)	Fluorescence[c] data (λ_{max} (nm))
1	373[a], 290[b]	458
2	364[a], 266[b]	498
3	373[a], 282[b]	476

[a] LMCT.
[b] $\pi \rightarrow \pi^*$.
[c] Exicitation at LMCT.

3.5. Cyclic voltammetry

The electrochemical properties of complexes **1**, **2**, **3** and the ligand HL were studied at a scan rate of 50 mV s^{-1}. The HL ligand

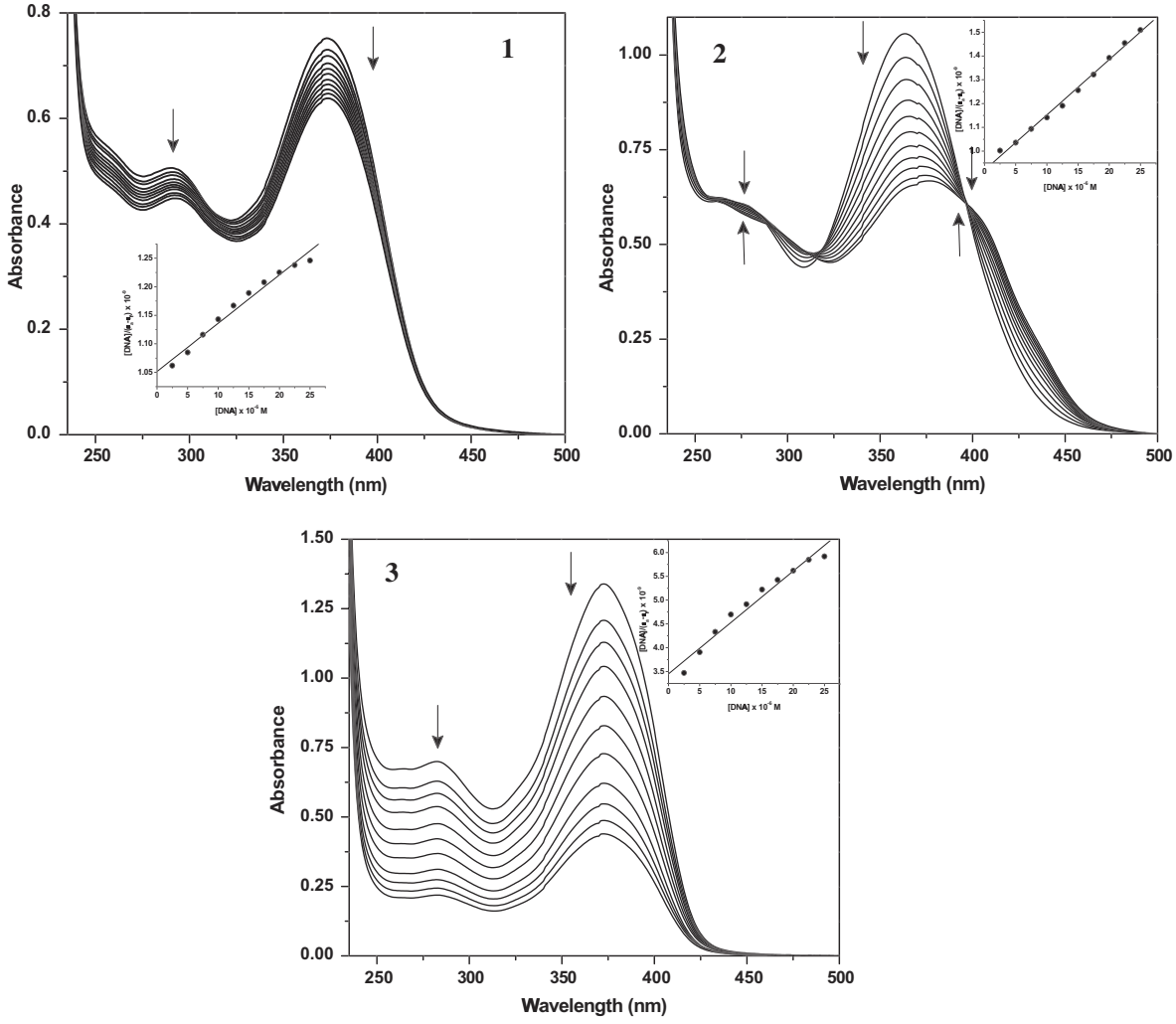

Fig. 4. Electronic absorption spectra of complexes **1**–**3** (25 μM) in the absence and presence of increasing amounts of CT DNA (2.5, 5.0, 7.5, 10.0, 12.5, 15.0, 17.5 and 20.0, 22.5 and 25 μM). Arrows show the changes in absorbance with respect to an increase in the DNA concentration (inset: plot of [DNA] versus [DNA]/($\varepsilon_a - \varepsilon_f$)).

is neither reduced nor oxidized reversibly in the potential range explored, hence the redox processes are assigned exclusively to the transition metals. Peaks corresponding to the potentials +1.211 V and 0.801 V were recorded for complex **1**. The anodic response detected at +1.211 V is believed to be due to Ni(II) → Ni(III) oxidation and the cathodic response at 0.801 V is attributable to Ni(III) → Ni(II) reduction. The large peak-to-peak separation (ΔE_P = 410 mV) and the observed i_c/i_a ratio due to cathodic and anodic sweeps at the scan rates employed (25–200 mV s^{-1}) implies that this process can be best regarded as a quasi-reversible oxidation. This behavior can be explained on the basis of slow electron transfer and to adsorption of the complexes onto the electrode surface [45]. The voltammogram for complex **2** exhibits an irreversible oxidation peak at 0.641 V which is attributable to the oxidation of Co(II) to Co(III). An additional peak detected at −0.303 V is assigned to the reduction of Co(II) to Co(I). Furthermore, complex **2** displays the corresponding oxidation peak at −0.181 V which is assignable to Co(I) to Co(II) oxidation. This process is completely reversible and is characterized by a peak-to-peak separation (ΔE_p) of 122 mV. The cyclic voltammogram for complex **3** exhibits a reduction peak at −0.307 V which is assigned to the reduction of Cu(II) to Cu(I). The corresponding oxidation peak is not observed, thus implying that the hydrazone ligand stabilizes the +1 oxidation state of Cu. The potential difference ($\Delta E_p = Ep_a - Ep_c$) of the first electrode couple increases with increasing scan rates. This behavior has been reported for related complexes, thus confirming the occurrence of a slow chemical reaction pursuant to the electrode process [46].

3.6. DNA binding

3.6.1. Absorption titration of the copper complex bound to DNA

Any change in the UV–Vis absorption spectra of metal complexes upon the addition of DNA serve as an evidence for the existence of an interaction between them. In particular, hypochromism due to $\pi \rightarrow \pi^*$ stacking interaction with a red-shift (bathochromism) may appear in the case of an intercalative binding leading to stabilization of DNA duplex [47]. The electronic absorption spectra of complexes **1**, **2** and **3** exhibited two well-resolved bands in the range of 200–400 nm. Upon the addition of DNA, the band at 290 nm for the complex **1** exhibited hypochromism of about 11.40% together with 2 nm red shift and the band at 373 nm (complex **1**) showed only hypochromism (15.15%) without any shift. On the other hand, the band centered at 266 nm corresponding to complex **2** exhibited a slight hyperchromism during the initial stages of DNA addition suggesting the tight binding and stabilization whereas further addition of DNA results in a hypochromism indicating the strong binding to CT DNA probably by intercalation. Additionally, the band at 364 nm showed a hypochromism (37%) accompanied with red-shift of 5 nm. A distinct isobestic point

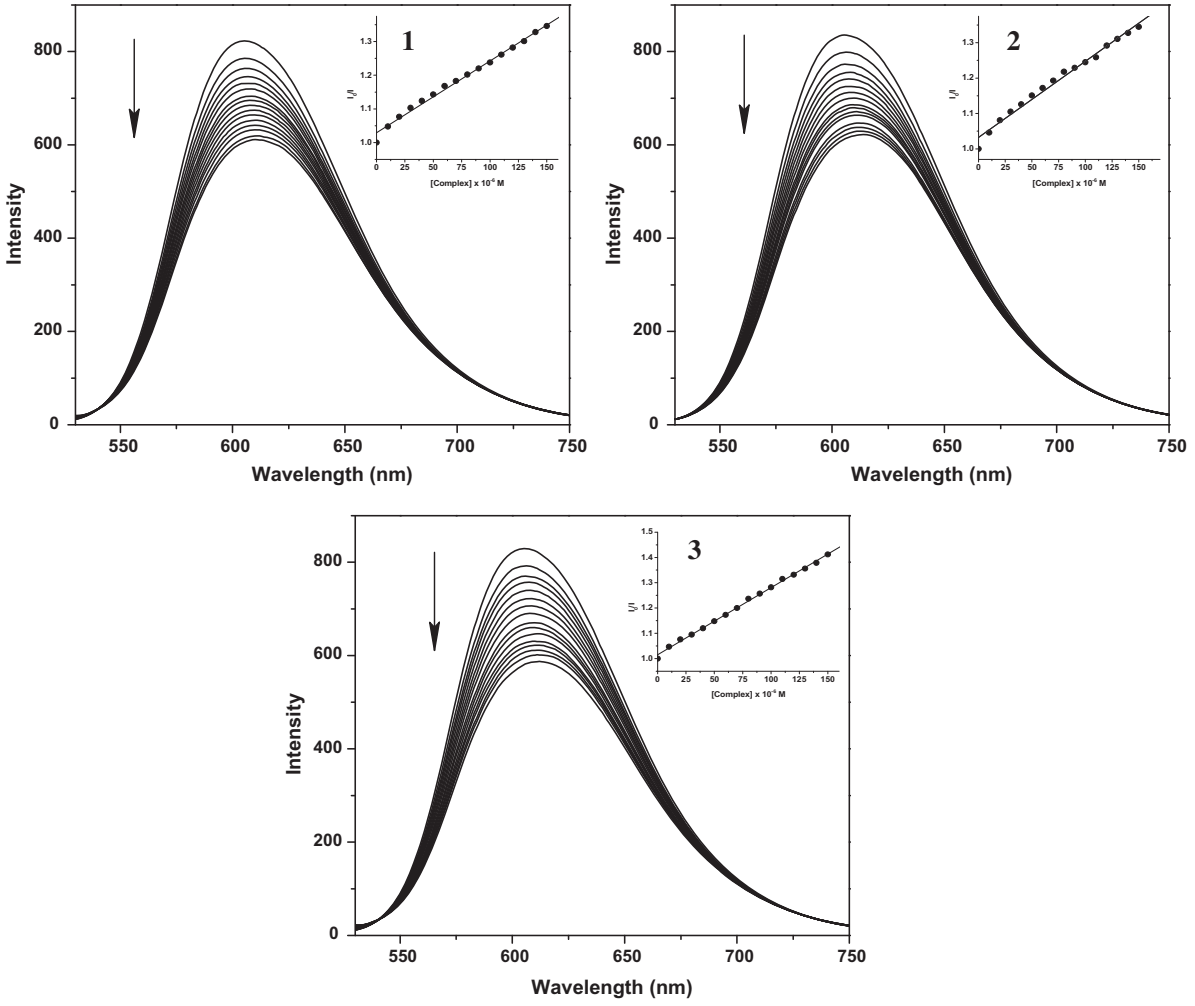

Fig. 5. Emission spectra of DNA–EB, in the presence of 0, 10, 20, 30, 40, 50, 60, 70, 80, 90, 100, 110, 120, 130, 140 and 150 μM of complexes **1**–**3**. Arrow indicates the changes in the emission intensity as a function of complex concentration. Inset: Stern–Volmer plot of the fluorescence titration data corresponding to the complexes **1**–**3**.

observed at 397 nm which indicates the existence of single mode of binding. However, the band at 282 nm for complex **3** exhibited hypochromism (68.72%) together with 1 nm red shift and the band at 373 nm also showed hypochromism of about 67.20% without any shift in wavelength. The observed hypochromism could be attributed to stacking interaction between the aromatic chromophores of the complexes and DNA base pairs consistent with the intercalative binding mode, while the red-shift is an evidence of the stabilization of the CT DNA duplex. UV–Vis spectra of metal complexes in the absence or presence of CT DNA derived for diverse *R* values are shown representatively for complexes **1**, **2** and **3** in Fig. 4.

In order to compare quantitatively the binding ability of the three different complexes containing same hydrazone ligand but different metal ions with CT DNA, the intrinsic binding constants were determined by monitoring the changes in lower energy bands of complexes **1**, **2** and **3**, respectively, with increasing concentration of DNA using the equation: $[DNA]/[\varepsilon_a - \varepsilon_f] = [DNA]/[\varepsilon_b - \varepsilon_f] + 1/K_b[\varepsilon_b - \varepsilon_f]$; [DNA] versus $[DNA]/[\varepsilon_b - \varepsilon_f]$ (shown in Fig. 4 as insets) gave a slope and the intercept which are equal to $1/[\varepsilon_a - \varepsilon_f]$ and $(1/K_b)[\varepsilon_b - \varepsilon_f]$, respectively; K_b is the ratio of the slope to the intercept. The magnitudes of intrinsic binding constants (K_b) were calculated to be $8.045 \times 10^3\ M^{-1}$, $2.528 \times 10^4\ M^{-1}$, and $3.135 \times 10^4\ M^{-1}$ corresponding to complexes **1**, **2** and **3**, respectively. The observed binding constant (K_b) revealed that the complex **3** containing copper ion is strongly bound with CT DNA than the other complexes containing nickel and cobalt ions as transition metal counterpart, respectively.

3.6.2. Competitive studies with ethidium bromide

Ethidium bromide (EB) serves as a typical indicator of intercalation since it can form soluble complexes with nucleic acids emitting intense fluorescence in the presence of CT DNA due to the intercalation of the planar phenenthridinium ring between adjacent base pairs on the double helix. EB does not show any appreciable emission in buffer solution due to fluorescence quenching of the free EB by the solvent molecules and the fluorescence intensity is highly enhanced upon addition of CT DNA, due to its strong intercalation with DNA base pairs. Addition of a second molecule (complex in our case), that may bind to DNA more strongly than EB results in lowering of DNA-induced EB emission intensity. The changes observed in the fluorescence spectra of EB on its binding to CT DNA are often used for the interaction study between DNA and other compounds, such as metal complexes.

The emission spectra of EB bound to CT DNA in the absence and presence of each compound have been recorded for [EB] = 10 μM and [DNA] = 10 μM upon the addition of increasing amounts of respective metal hydrazone complex [0–150 μM]. In the case of all the complexes **1, 2** and **3**, the addition with respect to different *R* values (Fig. 5) showed a significant decrease in the intensity of the emission band of the DNA–EB system at 604 nm of about 24.65%, 26.69% and 29.17% with red shift of 5 nm, 7 nm and 8 nm, respectively, indicates that there existed a competition between the metal hydrazone complexes and EB towards binding to DNA. The observed significant quenching of DNA–EB fluorescence after the addition of the complexes **1, 2** and **3** proved that they displace EB from the DNA–EB complex and they probably interact with CT DNA by the intercalative mode [48]. The quenching constant (K_q), obtained from the slope of the plot [Q] versus I_0/I (shown as insets in Fig. 5) is used to evaluate the quenching efficiency for each compound according to the equation: $I_0/I = K_q[Q] + 1$. The Stern–Volmer plots of DNA–EB illustrate that the quenching of EB bound to DNA by the compounds **1**–**3** is in good agreement with the linear Stern–Volmer equation. Further, the values of K_q corresponding to the three complexes are found as $2.070 \times 10^3\ M^{-1}$, $2.083 \times 10^3\ M^{-1}$ and $2.610 \times 10^3\ M^{-1}$, respectively. The K_{app} values obtained for the three different complexes using the equation $K_{EB}[EB] = K_{app}[complex]$ was found as $2.193 \times 10^5\ M^{-1}$, $2.222 \times 10^5\ M^{-1}$ and $2.692 \times 10^5\ M^{-1}$. These values suggested that the complex **3** containing bivalent copper ion showed higher quenching efficiency than the respective nickel and cobalt counterparts. However, neither the free hydrazone ligand nor the starting precursor complexes displayed any affinity towards CT DNA signifying the presence of metal ions in the hydrazone chelates is solely responsible for the kind of interaction exhibited by them. The binding as well as quenching constants determined in our experiments clearly demonstrates that the titled complexes possess better DNA interaction than other similar complexes reported in the literature [48].

3.7. DNA cleavage

Gel electrophoresis is a technique that is based on the migration of DNA under the influence of an electric potential. There are number of agents which exert their effect by inhibiting enzymes that act upon DNA. These inhibitions result from the binding of such agents to the enzyme site of interaction on the DNA rather than to direct enzyme inactivation. Transition metals have been reported to inhibit DNA repair enzymes. The DNA cleavage efficiency of the complex is attributed to the different binding affinity of the complex to DNA.

For comparison purposes, the cleavage reactions for **1**, **2** and **3** were carried out in the presence of H_2O_2 at a concentration of 35 μM. Each complex was found to possess nuclease activity. Control experiments carried out using DNA or mixtures of H_2O_2 and DNA do not show any apparent cleavage of DNA as is evident in lanes 1 and 2, respectively (Fig. 6A). The cleavage efficiencies for complexes **1**, **2** and **3** (lanes 3, 4 and 5, respectively; Fig. 6A) in the presence of H_2O_2 are sufficient to exhibit nuclease activity. Based upon their ability to convert the supercoiled form (Form I SC) to the nicked circular (Form II NC), complex **3** was found to be an efficient chemical nuclease for double strand cleavage of

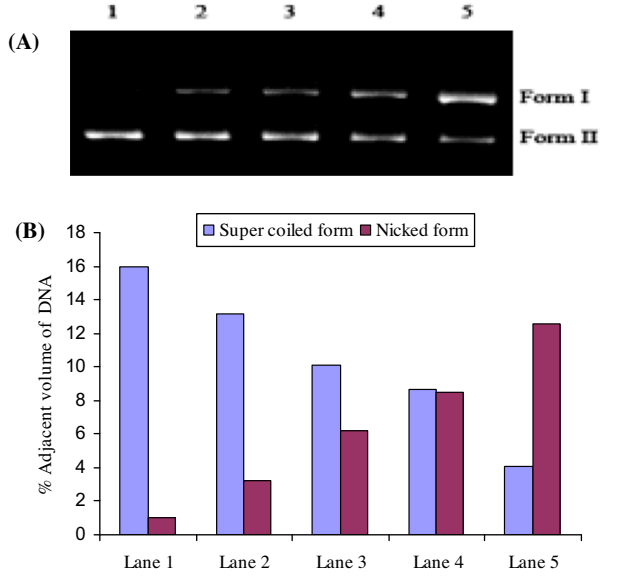

Fig. 6. (A) Gel-electrophoresis pictures for the metal hydrazone complexes Photograph showing the effects of transition metal hydrazones on DNA of pUC19: Lane 1: SC pUC19 DNA (0.5 μg) alone; Lane 2: SC pUC19 DNA (0.5 μg) + H_2O_2(60 μM); Lane 3: SC pUC19 DNA (0.5 μg) + H_2O_2(60 μM) + (**1**)(30 μM); Lane 4: SC pUC19 DNA (0.5 μg) + H_2O_2(60 μM) + (**2**)(30 μM); Lane 5: SC pUC19 DNA (0.5 μg) + H_2O_2(60 μM) + (**3**)(30 μM). (B) Relative amounts of different DNA forms in the presence of complexes **1**, **2** and **3**.

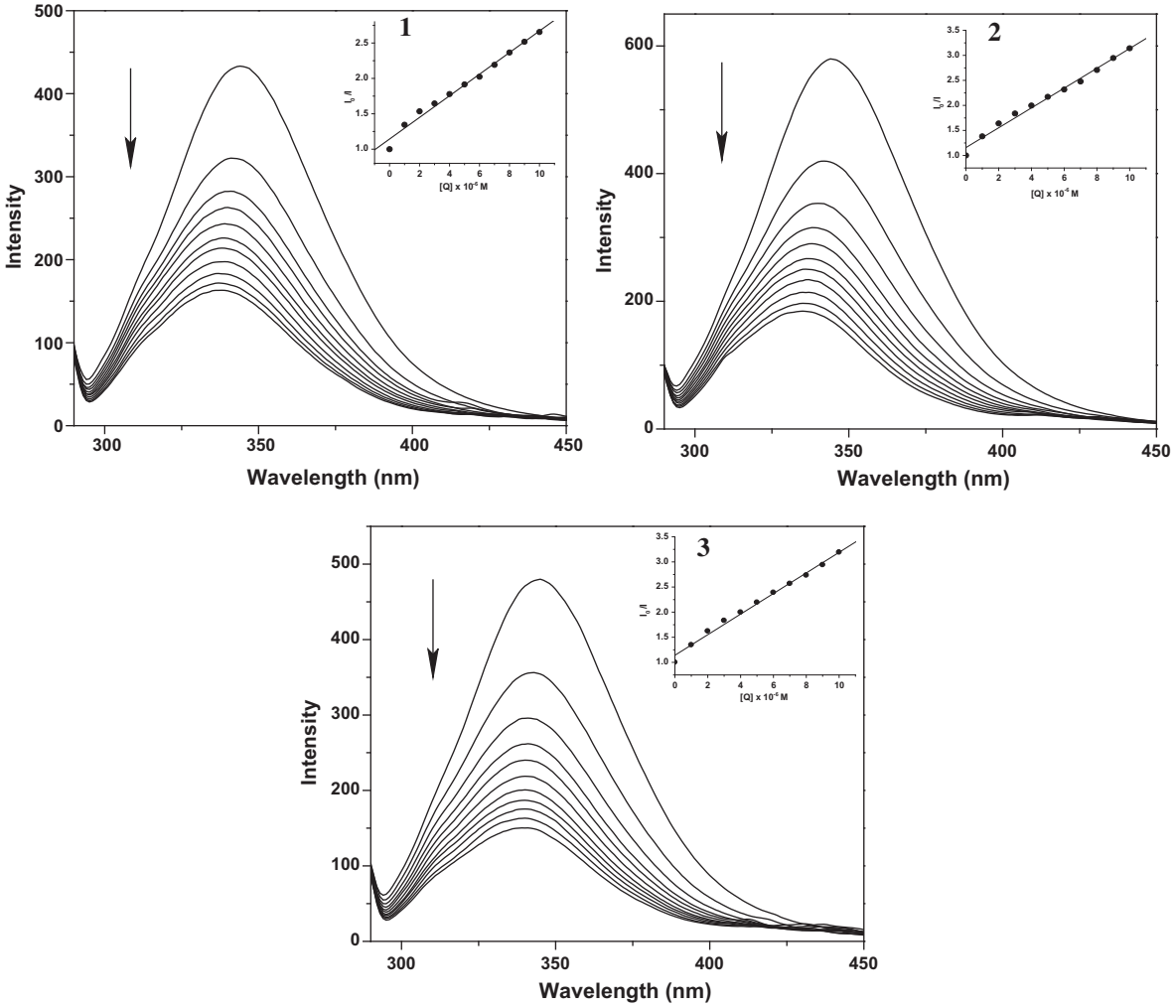

Fig. 7. Emission spectrum of BSA (1×10^{-6} M; λ_{exi} = 280 nm; λ_{emi} = 345 nm) as a function of concentration of the complexes **1**–**3** (1, 2, 3, 4, 5, 6, 7, 8, 9 and 10×10^{-6} M). Arrow indicates the effect of metal complexes on the fluorescence emission of BSA. (Inset: Stern–Volmer plot of the fluorescence titration data corresponding to the complex **1**–**3**).

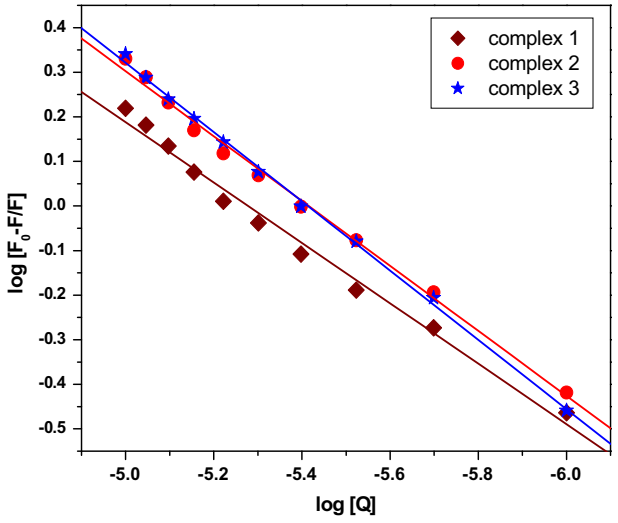

Fig. 8. Plot of log $[(F_0 - F)/F]$ versus log $[Q]$ for complexes **1**, **2** and **3**.

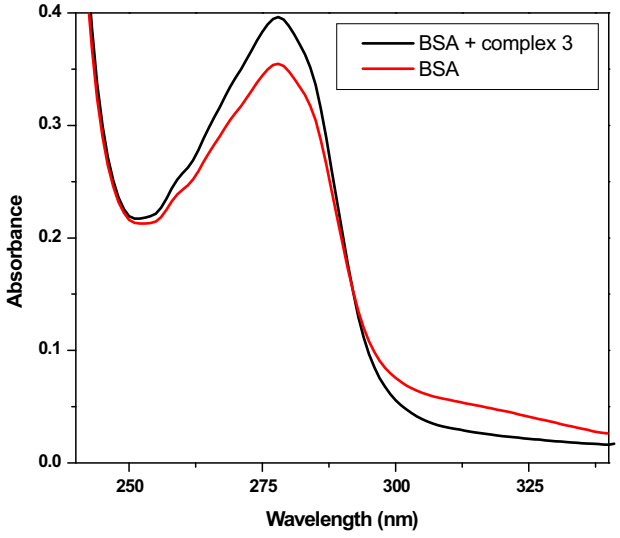

Fig. 9. The absorption spectra of BSA (1×10^{-5} M) and BSA–complex **3** (BSA = 1×10^{-5} M and Complex **3**= 1×10^{-6} M).

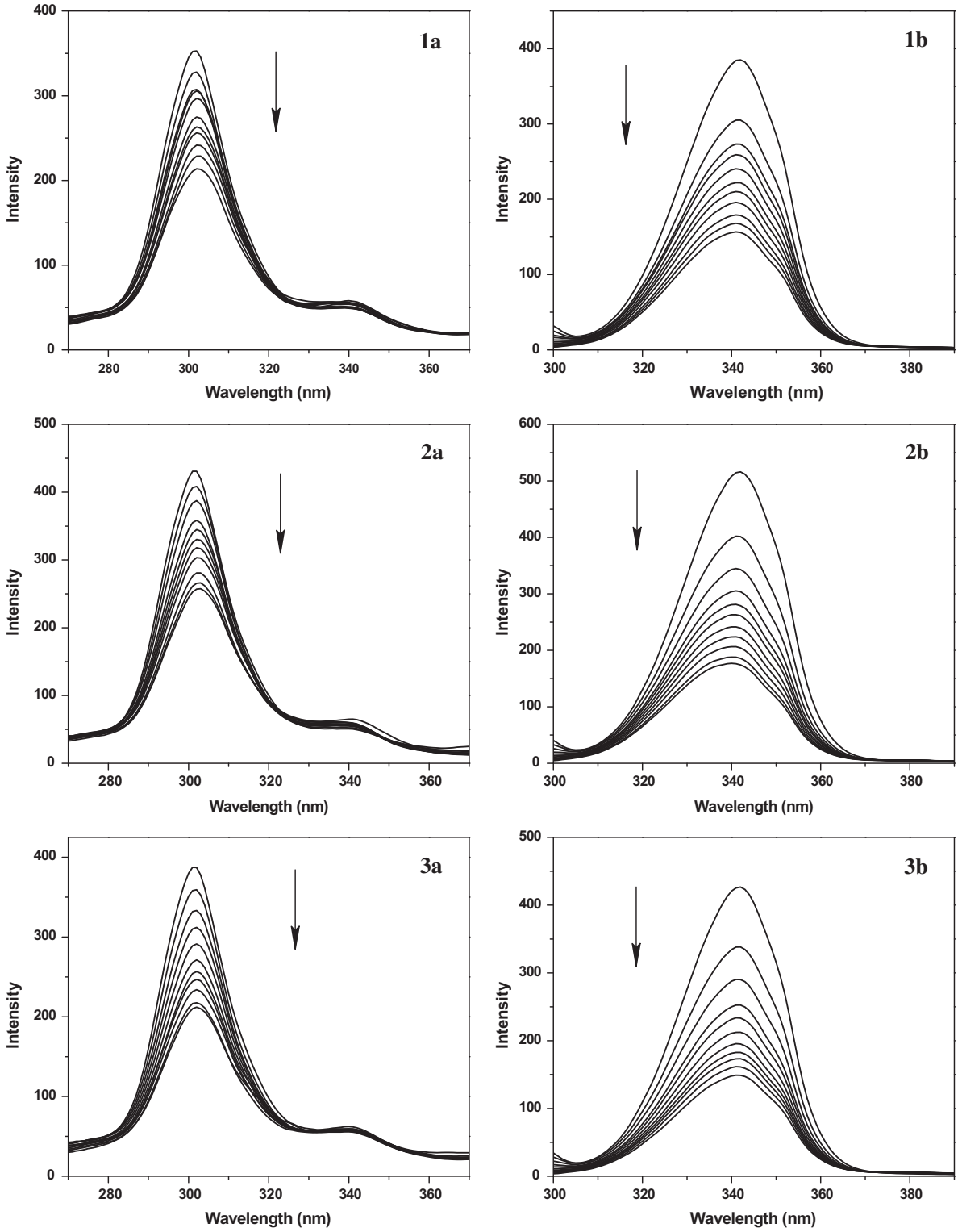

Fig. 10. Synchronous spectra of BSA (1×10^{-6} M) as a function of concentration of the complexes **1**–**3** (0, 1, 2, 3, 4, 5, 6, 7, 8, 9 and 10×10^{-6} M) with wavelength difference of $\Delta\lambda$ = 15 nm (a) and $\Delta\lambda$ = 60 nm (b). Arrow indicates the changes in emission intensity w.r.t various concentration of complexes **1**–**3**.

DNA in comparison with complexes **1** and **2**. The foregoing observations suggest that cleavage of the supercoiled form and formation of the nicked circular form increased in the order **1< 2< 3** (Fig. 6B). It is believed that the superior cleavage ability of the copper complex is due to the reaction of copper ions with H_2O_2, which produces diffusible hydroxyl radicals or molecular oxygen, which in turn damage DNA through Fenton-type chemistry [49].

3.8. Protein binding studies

3.8.1. Fluorescence quenching of BSA by metal complexes

BSA molecule contains three aromatic amino acids (phenylalanine, tyrosine and tryptophan) and the fluorescence of BSA can appear because of tryptophan and tyrosine residues [50]. If the protein conformation changes, it will lead to the fluorescence

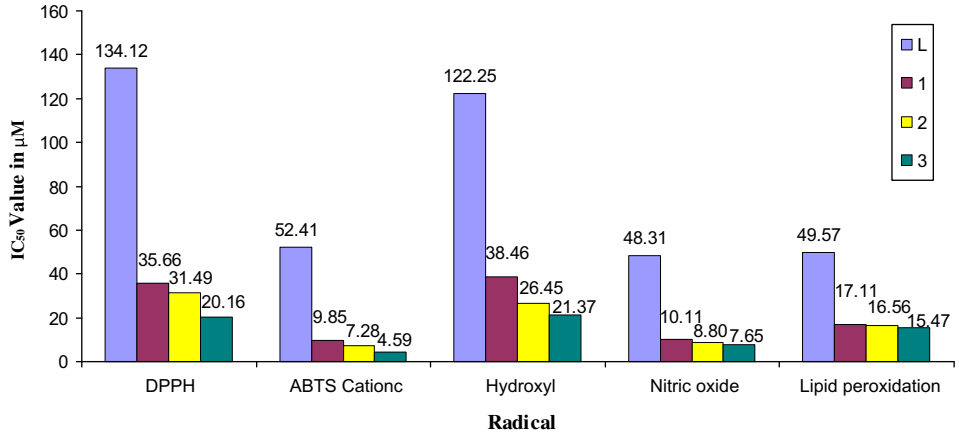

Fig. 11. Trends in the inhibition of DPPH·, $ABTS^{\cdot+}$, OH·, NO and lipid peroxidation by ligand **L** and complexes **1**, **2** and **3**.

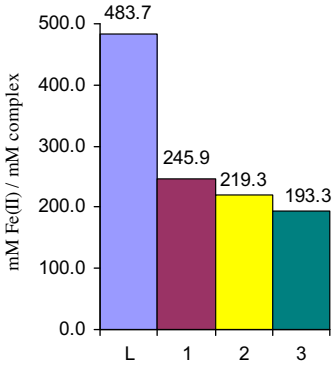

Fig. 12. Ferric reducing antioxidant power (FRAP) of ligand **L** and complexes **1**, **2** and **3**.

emission change [51]. Fig. 7 shows the effect of increasing the concentration of metal complexes on the fluorescence emission of BSA. Addition of metal complexes to the solution of BSA resulted in the quenching of its fluorescence emission with blue shift suggesting that the complex formed between the metal hydrazones and BSA is responsible for the quenching of BSA. The fluorescence quenching is described by Stern–Volmer relation: $I_0/I = 1 + K_{SV}[Q]$; where I_0 and I are the fluorescence intensities of the fluorophore in the absence and presence of quencher, respectively, K_{SV} is the Stern–Volmer quenching constant and [Q] is the quencher concentration. The K_{SV} value obtained from the plot of [Q] versus I_0/I (shown in Fig. 7 as insets) was found to be $1.528 \times 10^5\ M^{-1}$, $1.979 \times 10^5\ M^{-1}$ and $2.049 \times 10^5\ M^{-1}$ corresponding to the complexes **1**, **2** and **3**, respectively.

When small molecules bind independently to a set of equivalent sites on a macromolecule, the equilibrium between free and bound molecules is represented by the Scatchard equation [52]: $\log[(F_0 - F)/F] = \log[K] + n\ \log[Q]$; where K and n are the binding constant and the number of binding sites, respectively. Binding constants obtained from the plot of $\log[Q]$ versus $\log[(F_0 - F)/F]$ (Fig. 8) corresponding to the complexes **1**, **2** and **3** were $3.754 \times 10^3\ M^{-1}$, $8.775 \times 10^3\ M^{-1}$ and $1.604 \times 10^4\ M^{-1}$, respectively .

3.8.2. UV–Vis absorption measurement of BSA by metal complexes

UV–Vis absorption measurement is a very simple and effective method in exploring the structural change and detecting the complex formation [53]. For confirming the type of quenching (i.e., static or dynamic) effect may exist in the system of metal hydrazones and BSA, the absorption spectra of BSA in the presence and absence of metal complex were recorded and a representative spectrum of complex **3** is presented in Fig. 9 which revealed that the absorbance intensity of BSA appeared at 280 nm has been increased after the addition of metal complex due to the formation of BSA–complex **3** [54]. Similar behavior was observed for other complexes and hence, these results confirm that static quenching exists in the interaction between BSA–complex.

3.8.3. Characteristics of synchronous fluorescence spectra

Since the synchronous fluorescence spectra can give information about the molecular environment in the vicinity of fluorophore functional groups, it is a useful method to evaluate the conformational changes of BSA. Moreover, it has several advantages, such as spectral simplification, spectral bandwidth reduction, and avoiding different perturbing effects. The shift in maximum emission position corresponds to the change in the polarity around the chromophore molecule. Thus, the environment of amino acid residues can be studied by measuring the shift in wavelength emission maximum. When the wavelength interval ($\Delta\lambda$) is 15 nm or 60 nm, the synchronous fluorescence offers the characteristic information of tyrosine residues or tryptophan residues [55]. The synchronous fluorescence spectroscopy of BSA upon addition of metal-complexes gained at $\Delta\lambda = 15$ nm and $\Delta\lambda = 60$ nm are shown in Fig. 10.

To investigate the structural changes occurred to BSA upon the addition of metal complexes **1**–**3**, we measured synchronous fluorescence spectra of BSA before and after the addition with respect to all the three complexes. From the spectra, we understand that an increase in the concentration of metal complexes resulted in a decrease in the intensity of the synchronous fluorescence spectral band corresponding to tyrosine residue with a slight red shift (1 nm), except in the case of complex **1** which displayed hypochromism only. In addition, a gradual decrease of fluorescence intensity of tryptophan residues together with a small blue shift (1 nm) in the emission wavelength were also observed after the addition all the three complexes to BSA. These experimental results indicate that the metal complexes do affect the microenvironment of both tyrosine and tryptophan residues during the binding process and synchronous measurements confirmed the effective binding of all the complexes with BSA. Similar behavior was observed for the interaction between the BSA and other metal complexes [56].

3.9. Antioxidant activity

The antioxidant activities of complexes **1**, **2** and **3** were evaluated in a series of *in vitro* assays involving DPPH radicals, ABTS

cationic radicals, hydroxyl radicals, nitric oxide radicals and on the basis of reducing power. The complexes were also studied for lipid peroxidation by thiobarbituric acid reactive substances (TBARS) using rat liver. The three complexes exhibited a scavenging effect at a fixed concentration of 50 μM.

IC_{50} values of the ligand (**L**) on DPPH, ABTS cationic, OH, NO radicals and lipid peroxidation assays are 134.12, 52.41, 122.25, 48.31 and 49.57 μM, respectively, whereas, the complexes **1, 2** and **3** showed their IC_{50} values at 35.66, 9.85, 38.46, 10.11, 17.11, 31.41, 7.28, 26.45, 8.80, 16.56, 20.16, 4.59, 21.37, 7.65 and 15.47 μM, respectively. The results of these experiments were shown in Fig. 11. In order to assess the ferric reducing abilities, the $Fe^{3+} \rightarrow Fe^{2+}$ transformation was investigated in the presence of **L** and **1**, **2** and **3**. The reducing capacity of a compound serves as a significant indicator of its potential antioxidant activity. The reductive effects of **L** and **1**, **2** and **3** are summarized in Fig. 12.

In general, the antioxidant activity of the ligand and its M(II) complexes [where M = Ni, Co and Cu] against the free radicals i.e., DDPH, ABTS cationic, NO, OH, FRAP and lipid peroxidation was found to decrease in the order of **3**> **2**> **1**>**L**. The results indicated that the metal complexes exhibited greater antioxidant activity than the free ligand. Among the tested complexes, complex **3** displayed very high scavenging activity due to the presence of Cu(II) ion as described in the previous section. Further, the results obtained against the different radicals confirmed that the complexes are more effective to arrest the formation of the ABTS than the other radicals studied. In addition, the results obtained in this study imply that the metal complexes possess excellent antioxidant activities that are superior to those of standard antioxidants such as butylated hydroxyl anisole (BHA) and quercetin. The observed lower IC_{50} values in antioxidant assays did demonstrate that these complexes have the potential as drugs to eliminate the radicals.

4. Conclusions

Three new octahedral complexes **1**, **2** and **3** supported by tridentate NNO donor hydrazone ligand derived from furoic acid hydrazide and 2-benzoyl pyridine have been synthesized and characterized by FT-IR and UV–Vis, photoluminescence spectroscopy and cyclic voltammetry. The new complexes were formed in 1:2 metal-to-ligand mole ratios. Single crystal XRD results of all the three complexes revealed an octahedral geometry around the metal ion with hydrazone as a monobasic tridentate ligand comprising azomethine nitrogen, an enolic oxygen and a pyridine nitrogen atom.

Studies on the binding of the titled complexes with both DNA and BSA reflect that they behaved as intercalators towards the former and selectively interacted with tyrosine and tryptophan moieties of the later. The DNA cleavage capabilities of complexes **1**, **2** and **3** in the presence of H_2O_2 revealed their potential nuclease activity to cleave the supercoiled form into the nicked form increased in the order **1**< **2**< **3**. The ligand **L** and metal complexes **1**–**3** were screened for their scavenging activities toward DPPH, the ABTS radical cation, the NO radical and the OH radical. The ferric reducing antioxidant power (FRAP) and the inhibition of iron(II)-induced lipid peroxidation at 50 μM concentration were also investigated. Of the three complexes, the complex **3** exhibited superior activities in terms of the ABTS radical cation, lipid peroxidation and NO radical scavenging assays. From the biological activity experiments, we concluded that the complex **3** containing copper metal ion exhibited more potential than the complexes **1** and **2** containing nickel and cobalt ions that can be correlated to the presence of biologically essential copper ion in the molecular environment.

Acknowledgments

We sincerely thank Dr. Abraham John, Gandhigram University, Gandhigram, India for carrying out the electrochemical measurements. We are also grateful to Prof. S. Manian, Department of Botany, Bharathiar University for his help with the biological activity studies. We also offer our sincere thanks to the University Grants Commission, New Delhi for the award of Research Fellowship in Science for Meritorious Students (RFSMS) to one of the authors (P. Krishnamoorthy) under the UGC–SAP–DRS programme. AHC is grateful to the Robert A. Welch Foundation (Grant No. F-0003) for financial support of this work.

Appendix A. Supplementary material

CCDC 787858, 796257 and 779830 contain the supplementary crystallographic data for this paper. These data can be obtained free of charge from The Cambridge Crystallographic Data Centre via www.ccdc.cam.ac.uk/data_request/cif. Supplementary data associated with this article can be found, in the online version, at doi:10.1016/j.ica.2011.11.033.

References

[1] L. Ranconi, P.J. Sadler, Coord. Chem. Rev. 251 (2007) 1633.
[2] T. Storr, K.H. Thompson, C. Orvig, Chem. Soc. Rev. 35 (2006) 534.
[3] Z. Guo, P.J. Sadler, Angew. Chem., Int. Ed. 38 (1999) 1512–1531.
[4] G.I. Miessler, D.A. Tarr, Inorganic Chemistry, third ed., Prentice Hall, 2003, p. 299.
[5] S. Chandra, X. Sangeethika, Spectrochim. Acta A 60 (2004) 147.
[6] E. Kimura, S. Wada, M. Shiyonoya, Y. Okazaki, Inorg. Chem. 33 (1994) 770.
[7] B. De Clercq, F. Verpoort, Macromolecules 35 (2002) 8943.
[8] D.K. Johnson, T.B. Murphy, N.J. Rose, W.H. Goodwin, L. Pickart, Inorg. Chim. Acta 67 (1982) 159.
[9] E. Meggers, Curr. Opin. Chem. Biol. 11 (2007) 287–292.
[10] J.K. Barton, Science 233 (1986) 727.
[11] J.C. Francois, T. Saison-Behmoaras, M. Chassignol, N.T. Thuong, J.S. Sun, C. Helene, Biochemistry 27 (1988) 2272.
[12] Q. Guo, M. Lu, N.C. Seeman, N.R. Kallenbach, Biochemistry 29 (1990) 570.
[13] N. Zhou, Y.Z. Liang, P. Wang, J. Mol. Struct. 872 (2008) 190.
[14] J.H. Tang, F. Luan, X.G. Chen, Bioorg. Med. Chem. 14 (2006) 3210.
[15] K.S. Ghosh, S. Sen, B.K. Sahoo, S. Dasgupta, Biopolymers 91 (2009) 737.
[16] Yong Li, Zheng-yin Yang, J. Inorg. Biochem. 362 (2009) 4823.
[17] M. Caacelli, P. Mazza, C. Pelizzi, G. Pelizzi, F. Zani, J. Inorg. Biochem. 57 (1995) 43.
[18] Yong-chun Liu, Zheng-yin Yang, J. Inorg. Biochem. 103 (2009) 1014.
[19] S. Banerjee, S. Mondal, W. Chakraborty, S. Sen, R. Gachhui, R.J. Butcher, A.M.Z. Slawin, C. Mandal, Samiran Mitra, Polyhedron 28 (2009) 2785.
[20] J. Venanzi, J. Chem. Soc. (1958) 719.
[21] G.N. Rao, Ch. Janardhana, K. Pasupathy, P. Mahesh Kumar, Ind. J. Chem. 39B (2000) 151.
[22] A.A.R. Despaigne, J.G.D. Silva, A.C.M. do Carmo, O.E. Piro, E.E. Castellano, H. Beraldo, Inorg. Chim. Acta 362 (2009) 2117.
[23] P. Krishnamoorthy, P. Sathyadevi, K. Senthil Kumar, P. Thomas Muthiah, R. Ramesh, N. Dharmaraj, Inorg. Chem. Commun. 14 (2011) 1318.
[24] G.M. Sheldrick, SHELXTL-PC, Version 5.03, Siemens Analytical X-ray Instruments Inc., Madison, Wisconsin, USA, 1994.
[25] G.M. Sheldrick, Acta Crystallogr., Sect. A 64 (2008) 112.
[26] A.L. Spek, Acta Crystallogr., Sect. A 46 C34 (1990).
[27] H. Chao, W. Mei, Q. Huang, L. Ji, J. Inorg. Biochem. 92 (2002) 165.
[28] M. Lee, A.L. Rhodes, M.D. Wyatt, S. Forrow, J.A. Hartley, Biochemistry 32 (1993) 4237.
[29] J. Bernadou, G. Pratviel, F. Bennis, M. Girardet, B. Meunier, Biochemistry 28 (1989) 7268.
[30] M.S. Blois, Nature 29 (1958) 1199.
[31] R. Re, N. Pellegrini, A. Proteggente, A. Pannala, M. Yang, C. Rice-Evans, Free Radic. Biol. Med. 26 (1999) 1231.
[32] R. Pulido, L. Bravo, F. Saura-Calixto, J. Agric. Food Chem. 48 (2000) 3396.
[33] T. Nash, Biochem. J. 55 (1953) 416.
[34] L.C. Green, D.A. Wagner, J. Glogowski, P.L. Skipper, J.S. Wishnok, S.R. Tannenbaum, Anal. Biochem. 126 (1982) 131.
[35] H.H. Draper, M. Hadley, Methods Enzymol. 186 (1990) 421.
[36] M. Yoshino, K. Murakami, Anal. Biochem. 257 (1998) 40.
[37] V. Suni, M.R.P. Kurup, M. Nethaji, Polyhedron 26 (2007) 3097.
[38] A.S. Pedrares, N. Camina, J. Romero, M.L. Duran, J.A.G. Vazquez, A. Sousa, Polyhedron 27 (2008) 3391.
[39] N.A. Mangalam, S. Sivakumar, M.R.P. Kurup, E. Suresh, Spectrochim. Acta A 75 (2010) 686.

[40] A. Sreekanth, H.K. Fun, M.R.P. Kurup, J. Mol. Struct. 737 (2005) 61.
[41] R. Dinda, P. Sengupta, S. Ghosh, T.C.W. Mak, Inorg. Chem. 41 (2002) 1684.
[42] P.B. Sreeja, M.R.P. Kurup, A. Kishore, C. Jasmin, Polyhedron 23 (2003) 575.
[43] Md. Abu Affan, S.W. Foo, I. Jusoh, S. Hanapi, E.R.T. Tiekink, Inorg. Chim. Acta 362 (2009) 5031.
[44] Y. Shen, Y. Zhang, Y. Li, X. Tao, Y. Wang, Inorg. Chim. Acta (2007) 1628.
[45] A.W. Wallace, W.R. Murphy Jr., J.D. Peterson, Inorg. Chim. Acta 166 (1989) 47.
[46] M.C. Hughes, D.J. Macero, Inorg. Chem. 13 (1974) 2739.
[47] A.M. Pyle, J.P. Rehmann, R. Meshoyrer, C.V. Kumar, N.J. Turro, J.K. Barton, J. Am. Chem. Soc. 111 (1989) 3053.
[48] P. Krishnamoorthy, P. Sathyadevi, A.H. Cowley, R.R. Butorac, N. Dharmaraj, Eur. J. Med. Chem. 46 (2011) 3376.
[49] A.Y. Louie, T.J. Meade, Chem. Rev. 99 (1999) 2711.
[50] K.A.-Z. Osama, I.K.A.-S.H. Othman, J. Am. Chem. Soc. 130 (2008) 10793.
[51] P. Sathyadevi, P. Krishnamoorthy, M. Alagesan, K. Thanigaimani, P. Thomas Muthiah, N. Dharmaraj, Polyhedron 2011, doi:10.1016/j.poly.2011.09.021.
[52] J.R. Lakowicz, Fluorescence Quenching: Theory and Applications. Principles of Fluorescence Spectroscopy, Kluwer Academic/Plenum Publishers, New York, 1999. pp. 53–127.
[53] S.Y. Bi, D.Q. Song, Y. Tian, X. Zhou, Z.Y. Liu, H.Q. Zhang, Spectrochim. Acta A 61 (2005) 629.
[54] P. Sathyadevi, P. Krishnamoorthy, R.R. Butorac, A.H. Cowley, N.S.P. Bhuvanesh, N. Dharmaraj, Dalton Trans. (2011) 9690.
[55] C.X. Wang, F.F. Yan, Y.X. Zhang, L. Ye, J. Photochem. Photobiol. A 192 (2007) 23.
[56] D. Senthil Raja, G. Paramaguru, N.S.P. Bhuvanesh, J.H. Reibenspies, R. Renganathan, K. Natarajan, Dalton Trans. (2011) 4548.